

Hybrid tensor network and neural network quantum states for quantum chemistry

Zibo Wu,^{†,‡} Bohan Zhang,^{†,‡} Wei-Hai Fang,[†] and Zhendong Li^{*,†}

[†]*Key Laboratory of Theoretical and Computational Photochemistry, Ministry of Education,
College of Chemistry, Beijing Normal University, Beijing 100875, China*

[‡]*Contributed equally to this work.*

E-mail: zhendongli@bnu.edu.cn

Abstract

Neural network quantum states (NQS) have emerged as a powerful and flexible framework for addressing quantum many-body problems. While successful for model Hamiltonians, their application to molecular systems remains challenging for several reasons. In this work, we introduce three innovations to overcome some of the key limitations. (1) We propose two novel ansätze that hybridize tensor network and neural network states for addressing initialization challenges and enhancing the expressivity of tensor networks. First, we develop a bounded-degree graph recurrent neural network (BDG-RNN) ansatz that leverages graph-based updates, enabling applications to molecular electronic structure problems. Second, we introduce restricted Boltzmann machine (RBM) inspired correlators to further enhance expressivity and improve accuracy, without dramatically modifying the underlying variational Monte Carlo (VMC) optimization framework. (2) We introduce a semi-stochastic algorithm for local energy evaluation, which significantly reduces computational cost while maintaining high accuracy. Combining these advances, we demonstrate that our approaches can achieve chemical accuracy in challenging systems, including the one-dimensional

hydrogen chain H_{50} , the iron–sulfur cluster $[\text{Fe}_2\text{S}_2(\text{SCH}_3)_4]^{2-}$, and a three-dimensional $3 \times 3 \times 2$ hydrogen cluster H_{18} . These methods are implemented in an open-source package - PYNQS (<https://github.com/Quantum-Chemistry-Group-BNU/PyNQS>) to advance NQS methodologies for quantum chemistry.

1 Introduction

Efficiently solving the electronic Schrödinger equation has long been a key challenge for quantum many-body physics and quantum chemistry. However, due to the exponential scaling with respect to the electronic degrees of freedom, only a limited number of systems can be solved exactly. Some standard methods for solving the electronic Schrödinger equation include second-order Møller–Plesset perturbation (MP2),¹ configuration interaction (CI),² coupled cluster (CC),³ and density functional theory (DFT).⁴ In addition to these deterministic methods, quantum Monte Carlo (QMC) approaches provide effective alternatives through stochastic sampling. QMC can be broadly classified into two categories: variational Monte Carlo (VMC),⁵ which is based on optimizing trial wavefunctions, and projector Monte Carlo,⁶ including diffusion MC (DMC),⁷ Green’s function Monte Carlo (GFMC),^{8,9} and auxilliary-field QMC (AFQMC),^{10,11} which relies on projecting the system’s wavefunction onto the ground state through stochastic processes.

Neural network quantum states (NQS) have emerged as a powerful tool to solve quantum many-body problems. This paradigm was first introduced by Carleo and Troyer,¹² who demonstrated the use of restricted Boltzmann machines (RBMs) to describe prototypical interacting spin models. NQS leverages the expressive power of deep learning architectures to encode complex entanglement patterns.¹³ Since then, various deep learning architectures, including recurrent neural networks (RNNs),^{14,15} convolutional neural networks (CNNs),¹⁶ autoregressive NNs (ARNNs),^{17,18} Transformers,^{19–21} and retentive networks,²² have been integrated into NQS, further extending their applicability to quantum many-body systems. Although NQS have demonstrated remarkable progress in quantum many-body physics,

several critical challenges persist in practical applications to molecular electronic structure problems in quantum chemistry:

(1) One challenge arises from the limitations of NQS ansätze. The great flexibility of NQS without any physical constraint can exhibit a pronounced sensitivity to parameter initialization, particularly in large-scale strongly correlated systems. Recent methodological advances have addressed this challenge through diverse pretraining strategies, including the use of configuration interaction single and double excitations (CISD) wavefunction²³ and matrix product states (MPS).²⁴ Another promising direction, which is closely related with the present study, is to integrate with tensor network states^{15,18,25} to encoding more physical information into the wavefunction ansätze. For instance, Wu et al.¹⁵ introduced the MPS–RNN ansatz, which generalizes RNN to exactly represent MPS and extended this framework to two-dimensional (2D) systems via a multilinear memory update. However, the complexity of complex molecular systems can significantly exceed the simple 2D representations.

(2) Efficient optimization strategies remain critical for advancing NQS performance. Recent advances in non-stochastic optimization leverage selected configuration interaction (SCI) methods to deterministically select samples, yielding high-quality molecular energies through RBM^{26,27} and neural network backflow (NNBF) ansatz.^{23,28}

(3) A critical challenge for applying NQS to quantum chemistry lies in the high computational cost, as local energy evaluations dominate the computational workload in the NQS. While calculating local energies only within the sample space is a common approximation, this method can become inadequate for strongly correlated systems.^{17,20,29} An alternative strategy involves reducing computational complexity through efficient screening of matrix elements.^{30–32}

In this work, we introduce several advancements to overcome some of these limitations. First, building upon the MPS–RNN framework, we propose a bounded-degree graph RNN (BDG–RNN) architecture suitable for molecular electronic structure problems. Similar to MPS–RNN, BDG–RNN retains the use of MPS initial parameters, which avoids optimiza-

tion inefficiencies caused by random initialization. Second, we propose an RBM-inspired correlator architecture to further enhance the accuracy of NQS, while maintaining full compatibility with existing sampling frameworks. Finally, to reduce high computational costs in large-scale systems, we develop an efficient semistochastic scheme for local energy evaluation. The remainder of this article is organized as follows. In Section 2, we first present an overview of the VMC algorithm, followed by a detailed description of the BDG–RNN ansatz, the RBM-inspired correlator, and semistochastic local energy evaluation algorithm. In Section 3, we provide a brief description of the implementation and computational details. In Section 4, we apply the proposed methods in prototypical molecular systems, including the 1D hydrogen chain, an active space model of the iron–sulfur cluster $[\text{Fe}_2\text{S}_2(\text{SCH}_3)_4]^{2-}$, and the three-dimensional $3 \times 3 \times 2$ hydrogen cluster H_{18} . Finally, conclusions and future prospects of the NQS methodologies are discussed in Section 5.

2 Hybrid tensor network and neural network quantum states

2.1 Overview of VMC and NQS

Our goal is to solve the electronic Schrödinger equation in the second quantization

$$\hat{H}|\Psi\rangle = E|\Psi\rangle, \quad (1)$$

where

$$\hat{H} = \sum_{pq} h_{pq} \hat{a}_p^\dagger \hat{a}_q + \frac{1}{4} \sum_{pqrs} \langle pq||rs \rangle \hat{a}_p^\dagger \hat{a}_q^\dagger \hat{a}_s \hat{a}_r, \quad (2)$$

with h_{pq} and $\langle pq||rs \rangle$ being one-electron and two-electron molecular integrals, respectively, $\hat{a}_p^{(\dagger)}$ being the Fermionic annihilation (creation) operator for the p -th spin orbital. Any

quantum state $|\Psi\rangle$ can be expressed as the linear combination of the basis vectors

$$|\Psi\rangle = \sum_{n_1 \cdots n_{2K}} |n_1 n_2 \cdots n_{2K}\rangle C_{n_1 n_2 \cdots n_{2K}} \quad (3)$$

where $|n_1 n_2 \cdots n_{2K}\rangle$ represents the occupation number vectors (ONV) with $(n_i) \in \{0, 1\}^{2K}$, K is the total number of spatial orbitals, and $C_{n_1 n_2 \cdots n_{2K}}$ is the corresponding coefficients. The VMC algorithm is designed to approximate the ground state of a Hamiltonian by optimizing a parametrized trial wavefunction Ψ_θ with parameters θ . When Ψ_θ is implemented using a neural network, this ansatz is so-called NQS $|\Psi_\theta\rangle$. The energy E_θ of the trial state $|\Psi_\theta\rangle$ can be written as

$$E_\theta = \frac{\langle \Psi_\theta | \hat{H} | \Psi_\theta \rangle}{\langle \Psi_\theta | \Psi_\theta \rangle} = \langle E_{\text{loc}}(n) \rangle_{n \sim P_\theta(n)}, \quad (4)$$

where the probability distribution $P_\theta(n)$ is defined by

$$P_\theta(n) = \frac{|\langle \Psi_\theta | n \rangle|^2}{\sum_n |\langle \Psi_\theta | n \rangle|^2}, \quad (5)$$

and $E_{\text{loc}}(n)$ is the local energy

$$E_{\text{loc}}(n) = \sum_m H_{nm} \frac{\Psi_\theta(m)}{\Psi_\theta(n)}. \quad (6)$$

The matrix element H_{nm} is defined as $\langle n | \hat{H} | m \rangle$ where $|n\rangle$ is ONV. Sampling the ONV $|n\rangle$ according to $P_\theta(n)$ can be obtained using Markov chain Monte Carlo (MCMC)³³ or autoregressive sampling^{14,17} for ansätze having the autoregressive structure. The energy gradient with respect to parameters θ can be evaluated by

$$\partial_\theta E_\theta = 2\Re[\langle (\partial_\theta \ln \Psi_\theta^*(n))(E_{\text{loc}}(n) - \langle E \rangle) \rangle_{n \sim P_\theta(n)}], \quad (7)$$

where $\langle E \rangle$ is a shorthand notation for $\langle E_{\text{loc}}(n) \rangle_{n \sim P_\theta(n)}$, and $\partial_\theta \ln \Psi_\theta^*(n)$ can be calculated using automatic differentiation techniques.³⁴ The parameters θ are updated according to

$\partial_\theta E_\theta$ using an appropriate optimizer, such as stochastic gradient descent (SGD),³⁵ Adam,³⁶ and AdamW.³⁷

The accuracy of NQS relies heavily on the expressivity of the variational ansatz. The RBM wavefunction¹² represents one of the earliest variational NQS ansätze utilized for characterizing quantum states

$$\Psi_\theta(n) = e^{\sum_{j=1}^{N_v} a_j n_j} \times \prod_i^{N_h} 2 \cosh(b_i + \sum_{j=1}^{N_v} W_{ij} n_j), \quad (8)$$

where $\theta = \{(a_j), (b_i), (W_{ij})\}$ are the set of the real or complex network parameters. Here, N_h and N_v denote the number of hidden and visible units, respectively, and N_v typically corresponds to the number of spin orbitals. The “hidden variable density” α , defined as $\alpha = N_h/N_v$, can be adjusted to control the accuracy of the wavefunction.^{12,38,39}

The RNN wavefunction ansatz has the autoregressive structure,⁴⁰ which constructs the wavefunction through sequential conditional probability

$$\Psi(n) = \left(\prod_i \sqrt{P(n_t | n_{<t}^\circ)} \right) e^{i\phi(n)} \quad (9)$$

where $P(n_t | n_{<t}^\circ)$ represents the conditional probability. For the later convenience, we use $^\circ$ to indicate that the values of $n_{<t}$ are specified during the forward or sampling process. And $\phi(n)$ represents the phase of the wavefunction. The architecture operates through two key components at each step t : (1) The memory cell $h_t^{n_t} = \text{RNN}(h_{t-1}^{n_{t-1}^\circ}, n_{t-1}^\circ)$, where $h_t^{n_t^\circ} \in \mathbb{R}^x$ or \mathbb{C}^x for fixed t and specified n_t° , updated via RNN units that can encode historical information $h_{t-1}^{n_{t-1}^\circ}$, and (2) conditional wavefunction components consisting of amplitude $\sqrt{P(n_t | n_{<t}^\circ)}$ and phase ϕ_t , generated through two functions $f(h_t)$ and $g(h_t)$. For instance, the probability distribution can be computed as $P(n_t | n_{<t}^\circ) = n_t \cdot \text{softmax}(U^{(1)} h_t^{n_t} + c^{(1)})$ and the phase is calculated as $\phi_t = \pi \cdot \text{softsign}(U^{(2)} h_t^{n_t} + c^{(2)})$. Finally, the total phase is computed via $\phi(n) = \sum_t \phi_t$. The expressivity of RNN wavefunctions can be modulated by the choice of RNN architectures, such as GRU (Gated Recurrent Unit)⁴¹ and LSTM (Long

Short-Term Memory),⁴² as well as the form of the functions $f(h_t^{n_t})$ and $g(h_t^{n_t})$. By leveraging conditional probabilities, RNNs wavefunction can achieve accurate sampling through autoregressive sampling and avoid the inefficiency of MCMC.

Recently, Wu et al.¹⁵ reformulated the memory cell $h_t^{n_t}$ update to map MPS to RNN, see Fig. 1a. Suppose the tensor of MPS at the site t is denoted by $M_t^{n_t}$ ($(n_t) \in \{0, 1, 2, 3\}^K$), which is a χ -by- χ real/complex matrix for fixed t and specified n_t° . Then, the memory cell $h_t^{n_t}$ is

$$h_t^{n_t} = M_{t-1}^{n_t} h_{t-1}^{n_{t-1}^\circ} + v_t^{n_t}, \quad (10)$$

where $h_t^{n_t}$ and $v_t^{n_t} \in \mathbb{R}^\chi$ or \mathbb{C}^χ for fixed t and specified n_t° are vectors. The amplitude of wavefunction is defined through¹⁵ $P_t^{n_t} = (h_t^{n_t})^\dagger \eta_t h_t^{n_t}$, where η_t is a χ -by- χ non-negative diagonal matrix for fixed t . The phase component ϕ_t is computed via an additional linear transformation $\phi_t = \arg([w_t]^\text{T} h_t^{n_t^\circ} + c_t)$, where $w_t \in \mathbb{C}^\chi$ and $c_t \in \mathbb{C}$ for fixed t , and the total phase is computed via $\phi(n) = \sum_t \phi_t$. For the 2D case, the memory cell update is extended to incorporate interactions along both horizontal and vertical directions, see Fig.1b. The memory cell h_t at site t is computed as a combination of contributions from its horizontal h_{th} and vertical h_{tv} neighbouring cells

$$h_t^{n_t} = M_{th}^{n_t} h_{th}^{n_{th}^\circ} + M_{tv}^{n_t} h_{tv}^{n_{tv}^\circ} + v_t^{n_t}, \quad (11)$$

where $M_{th}^{n_t}$ and $M_{tv}^{n_t}$ are χ -by- χ parameter matrices acting on the horizontal and vertical directions for fixed t and specified n_t , respectively.

2.2 Bounded-degree graph RNN (BDG-RNN)

To describe the more complex entanglement among orbitals in molecules, we generalize MPS-RNN to BDG-RNN, see Fig. 1c, where memory cell updates are generalized beyond fixed horizontal/vertical dependencies to adaptively incorporate interactions defined by a bounded-degree graph (BDG). To generate the BDG, we first determine the ordering of

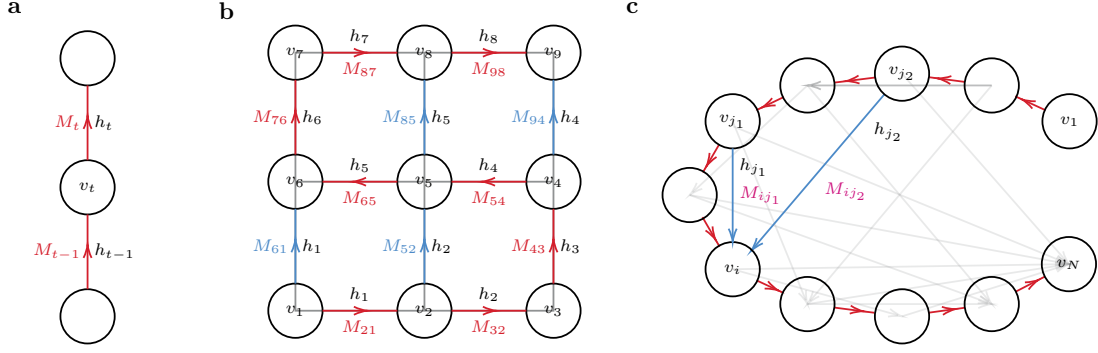


Figure 1: Different MPS-RNN wavefunction architectures: (a) the 1D MPS-RNN; (b) the 2D MPS-RNN with horizontal (red arrows) and vertical (blue arrows) memory cell interactions; (c) the BDG(k)-RNN featuring additional non-adjacent memory cell connections (blue arrows), where k denotes the out-degree constraint in bounded-degree graph. Each node corresponds to a spatial orbital, and the ordering of spatial orbitals is determined by the Fiedler ordering^{43,44} used in DMRG. Red arrows indicate the ordering of computations.

orbitals based on the exchange integral $K_{ij} = [ij|ji]$ between spatial orbitals i and j , using the Fiedler algorithm^{43,44} to construct a directed acyclic graph with a maximum out-degree constraint $k = 1$ excluding sources and sinks. Then, we add edges between a given vertex and other vertices via a greedy algorithm until the maximum out-degree k is reached. We summarize the processes in Algorithms S1 and S2, which transform the initial graph G into a modified graph G' with an maximum out-degree k . Based on the obtained graph G' , the BDG-RNN parameters can be structured through three fundamental components:

- Every vertex v_i maintains a memory cell $h_i^{n_i}$ with assigned parameters v_i, η_i, w_i, c_i .
- Every edge directed $v_j \rightarrow v_i$ is assigned a parameter matrix $M_{ij}^{n_i}$.
- If vertex v_i receives connections from multiple neighbors $\{v_\alpha, v_\beta, \dots, v_\gamma\}$, a tensor term $T_{i\alpha\beta\dots\gamma}^{n_i}$ is introduced.

Then, the memory cell $h_i^{n_i}$ is defined followed as:

$$\begin{aligned}
 h_i^{n_i} &= \text{RNN}(\{h_\alpha^{n_\alpha^\circ}\}_{\alpha \in \mathcal{N}(i)}) \\
 &= \sum_{\alpha \in \mathcal{N}(i)} M_{i\alpha}^{n_i} h_\alpha^{n_\alpha^\circ} + T_{i\alpha\beta\dots\gamma}^{n_i} \underbrace{h_\alpha^{n_\alpha^\circ} h_\beta^{n_\beta^\circ} \dots h_\gamma^{n_\gamma^\circ}}_{d \text{ items}} + v_i^{n_i},
 \end{aligned} \tag{12}$$

where $\mathcal{N}(i)$ denotes the neighborhood of vertex i . The tensor term $T_{i\alpha\beta\ldots\gamma}^{n_i}$ in Eq. 12 requires $\mathcal{O}(\chi^d)$ parameters, where d represents the in-degree of the vertex. To reduce the computational scaling, we adopt the Tucker decomposition⁴⁵ employed in Ref. ,¹⁵ viz.,

$$T_{i\alpha\beta\ldots\gamma}^{n_i} = U_{i'\alpha'\beta'\ldots\gamma'}^{n_i} \underbrace{K_{ii'} K_{\alpha\alpha'} K_{\beta\beta'} \ldots K_{\gamma\gamma'}}_{d \text{ items}}, \quad (13)$$

where U is rank- $(d+1)$ core tensor of shape (χ', \ldots, χ') , and $K_{ii'}$ are the corresponding factor matrices of shape (χ, χ') for each mode. We set $\chi' = \lceil \chi^{2/(d+1)} \rceil$ to perform the compression, which reduces the parameter complexity from $\mathcal{O}(\chi^d)$ to $\mathcal{O}(d\chi\chi' + \chi'^d)$. The amplitude $\sqrt{P_t}$ and phase ϕ_t components maintain the same computational structures to those in the vanilla MPS-RNN. We define two architectural variants based on Eq. 12: the BDG-RNN retaining without the tensor terms, and the BDG-TensorRNN incorporating both matrix and tensor terms. This unified framework allows for systematic transitions between different computational hierarchy: from 1D MPS-RNN to 2D MPS-RNN and finally to BDG(k)-RNN through controlled modifications of the BDG topology.

2.3 RBM-inspired correlators

To further improve the accuracy of NQS, we introduce an correlator in the following way

$$|\Psi_\theta\rangle = \sum_n f_n \Phi(n) |n\rangle, \quad \sum_n |\Phi(n)|^2 = 1, \quad (14)$$

where $\Phi(n)$ is a normalized NQS, f_n is an RBM-inspired correlator (vide post), and $|\Psi_\theta\rangle$ is not normalized. In this work, we employ two correlators inspired by the form of RBMs (8), which support volume-law entanglement.⁴⁶ First, we replace cosh with cos, and omit the exponential term $e^{\sum_{j=1}^{N_v} a_j n_j}$, thereby obtaining the following correlator

$$f_{\text{cos-RBM}}(n) = \prod_{k=1}^{N_h} \cos(b_k + \sum_{i=1}^{N_v} W_{ki} n_i), \quad (15)$$

which will be referred to as the cos-RBM correlator. Second, inspired by the work by Yang et al.,⁴⁷ we further introduce a quadratic term in the correlator,

$$f_{\text{Ising-RBM}}(n) = \prod_{k=1}^{N_h} \cos(b_k + \sum_{i=1}^{N_v} W_{ki}^{(1)} n_i + \frac{1}{2} \sum_{i,j=1}^{N_v} W_{kij}^{(2)} n_i n_j), \quad (16)$$

which will be referred to as the Ising-RBM in the later context. The parameter complexities of the cos-RBM and Ising-RBM scale as $\mathcal{O}(\alpha K^2)$ and $\mathcal{O}(\alpha K^3)$, respectively.

The energy for $|\Psi_\theta\rangle$ can be derived by reweighting⁴⁸ as

$$E_\theta = \frac{\langle \Psi_\theta | \hat{H} | \Psi_\theta \rangle}{\langle \Psi_\theta | \Psi_\theta \rangle} = \frac{\sum_n |\Phi(n)|^2 \frac{\langle \Psi_\theta | n \rangle \langle n | \hat{H} | \Psi_\theta \rangle}{|\Phi(n)|^2}}{\sum_n |\Phi(n)|^2 |f_n|^2} = \frac{\left\langle f_n^* \frac{\langle n | \hat{H} | \Psi_\theta \rangle}{\Phi(n)} \right\rangle_{n \sim |\Phi(n)|^2}}{\langle |f_n|^2 \rangle_{n \sim |\Phi(n)|^2}}. \quad (17)$$

Let $B = \langle |f_n|^2 \rangle_{n \sim |\Phi(n)|^2}$, we can redefine the local energy as

$$\begin{aligned} \tilde{E}_{\text{loc}}(n) &= \frac{f_n^* \langle n | \hat{H} | \Psi \rangle}{B \Phi(n)} = \frac{f_n^* \sum_m \langle n | \hat{H} | m \rangle \langle m | \Psi \rangle}{B \Phi(n)} = \sum_m \frac{f_n^*}{\sqrt{B}} \frac{f_m}{\sqrt{B}} \frac{H_{nm} \Phi(m)}{\Phi(n)} \\ &= \sum_m \tilde{f}_n^* H_{nm} \tilde{f}_m \frac{\Phi(m)}{\Phi(n)}, \end{aligned} \quad (18)$$

with $\tilde{f}_n = f_n / \sqrt{B}$, such that $E_\theta = \langle \tilde{E}_{\text{loc}}(n) \rangle_{n \sim |\Phi(n)|^2}$. The energy gradient can be derived as (see Supporting Information for details)

$$\partial_\theta E_\theta = 2\Re \left[\langle (\partial_\theta \ln(f_n \Phi(n)))^* (\tilde{E}_{\text{loc}} - |\tilde{f}_n|^2 \langle E \rangle) \rangle_{n \sim |\Phi(n)|^2} \right]. \quad (19)$$

Note that when $f_n \equiv 1$, both the energy and its gradient revert to the conventional VMC formulation, see Eq. (7). Moreover, the computational cost for evaluating these quantities remains comparable to the original method, with no significant overhead introduced.

2.4 Semistochastic algorithm for local energy

The standard algorithm for the local energy $E_{\text{loc}}(n)$ is via Eq. (6), which for the ab initio Hamiltonian (2) scales as $O(N_s K^4)$ for computing nonzero H_{nm} plus $O(N_s K^4)$ times the computational cost for computing $\Psi(n)$, with N_s being the (unique) sample size. For complex models such as NQS, the second part is dominant. Previous works^{17,20,29} often use an approximation that only computes the sum over m in the local energy Eq. (6) within the sample generated in VMC. However, this approximation introduces bias, which disappears only when the sample size goes to infinity. In this work, we propose a semistochastic algorithm to mainly reduce the computation of the second part. We use the Slater–Condon rules for evaluating the matrix elements H_{nm} , which are less time-consuming than the computation of the wavefunction, and hence we can decompose the local energy into two components based on the magnitude of H_{nm} : the *deterministic* part and the *stochastic* part. Specifically, the deterministic part $E_{\text{loc}}^{\text{d}}(n, \epsilon)$ involves summing over all the matrix elements H_{nm} that satisfy $|H_{nm}| \geq \epsilon$, ensuring that the contributions from these large terms are fully accounted for, viz.,

$$E_{\text{loc}}^{\text{d}}(n, \epsilon) = \sum_{\{m: |H_{nm}| \geq \epsilon\}} H_{nm} \frac{\Psi_{\theta}(m)}{\Psi_{\theta}(n)}. \quad (20)$$

This part is similar in spirit to that in Ref. ³² based on screening. However, only using this part will introduce a bias in the local energy.

The stochastic part $E_{\text{loc}}^{\text{s}}(n, \epsilon, N_{\epsilon})$ is designed to handle the smaller contributions by sampling m' from the distribution $P_n(m') \propto |H_{nm'}|$, where m' is defined by $|H_{nm'}| < \epsilon$. This part helps to reduce the computational cost for smaller terms, which would otherwise be computationally expensive. The number of samples denoted as N_{ϵ} is chosen based on the desired accuracy. Specifically, we can express the evaluation of the stochastic part by

$$E_{\text{loc}}^{\text{s}}(n, \epsilon, N_{\epsilon}) = \left\langle \frac{H_{nm'}}{P_n(m')} \frac{\Psi_{\theta}(m')}{\Psi_{\theta}(n)} \right\rangle_{m' \sim P_n(m')}. \quad (21)$$

Thus, the final local energy $E_{\text{loc}}(n)$ is evaluated as

$$E_{\text{loc}}(n, \epsilon, N_\epsilon) = E_{\text{loc}}^{\text{d}}(n, \epsilon) + E_{\text{loc}}^{\text{s}}(n, \epsilon, N_\epsilon), \quad (22)$$

where both ϵ and N_ϵ are the hyperparameters in this scheme. Unlike $E_{\text{loc}}^{\text{d}}(n, \epsilon)$, $E_{\text{loc}}(n, \epsilon, N_\epsilon)$ is an unbiased estimator for the energy. Note that when $\epsilon \rightarrow 0$ or $N_\epsilon \rightarrow \infty$, $E_{\text{loc}}(n, \epsilon, N_\epsilon)$ becomes the exact local energy (6). In practice, it is necessary to choose reasonably ϵ and N_ϵ in order to strike a balance between the variance and the computational complexity. We will illustrate this point for each molecules examined in this work.

3 Implementation and computational details

We implemented the above ansätze and semistochastic algorithm for local energy in an open-source package `PyNQS`⁴⁹ based on the PyTorch deep learning framework.⁵⁰ In addition to BDG-RNN, it also supports other commonly used NQS ansätze such as RBM and Transformers, and new ansätze can be easily added. The Hamiltonian matrix elements are evaluated using the Slater–Condon rules and hardware-efficient bitwise operation on graphics processing units (GPUs). To avoid out of memory, autoregressive sampling if BDG–RNN is implemented via a hybrid depth-first search (DFS) and breadth-first search (BFS) approach, as detailed in Algorithm S3. The BDG–RNN is initialized by using MPS generated from the `FOCUS`^{51,52} package. The molecular integrals are obtained using the `PySCF` package.⁵³ All variational parameters are optimized using the AdamW³⁷ algorithm with first- and second-moments set to $\beta_1 = 0.9$ and $\beta_2 = 0.999$, respectively. In this work, we use double precision (float64) for all the numerical data, but the program also supports single precision (float32) for reduced memory usage or improved performance when appropriate.

The BDG–RNN supports the use of two types of symmetries, particle number and spin projection, using the autoregressive structures. During the autoregressive sampling process,

the k -th spin orbitals must satisfy the following constraints:

$$\begin{aligned} N_\alpha - \left(\frac{N_e}{2} - \lfloor \frac{k}{2} \rfloor \right) &\leq \sum_{j=0}^{\lfloor \frac{k}{2} \rfloor} x_{2j} \leq N_\alpha \\ N_\beta - \left(\frac{N_e}{2} - \lfloor \frac{k}{2} \rfloor \right) &\leq \sum_{j=0}^{\lfloor \frac{k}{2} \rfloor} x_{2j+1} \leq N_\beta \end{aligned} \quad (23)$$

where $|x_0 x_1 \cdots x_{2K-1} x_{2K}\rangle = |n_{1\alpha} n_{1\beta} \cdots n_{K\alpha} n_{K\beta}\rangle$, N_α and N_β are the numbers of the α and β electrons, respectively. These physical constraints can be incorporated into the conditional probability distributions as follows²⁹

$$\tilde{P}(x_i | x_{i-1}, \dots, x_1) = \begin{cases} 1, & \text{if } N_\alpha - \left(\frac{N_e}{2} - \lfloor \frac{k}{2} \rfloor \right) > \sum_{j=0}^{\lfloor \frac{k}{2} \rfloor} x_{2j} \\ 1, & \text{if } N_\beta - \left(\frac{N_e}{2} - \lfloor \frac{k}{2} \rfloor \right) > \sum_{j=0}^{\lfloor \frac{k}{2} \rfloor} x_{2j+1} \\ 0, & \text{if } N_\alpha \leq \sum_{j=0}^{\lfloor \frac{k}{2} \rfloor} x_{2j} \\ 0, & \text{if } N_\beta \leq \sum_{j=0}^{\lfloor \frac{k}{2} \rfloor} x_{2j+1} \\ P(x_i | x_{i-1}, \dots, x_1), & \text{otherwise} \end{cases} \quad (24)$$

Note that after replacing $P(x_i | x_{i-1}, \dots, x_1)$ with $\tilde{P}(x_i | x_{i-1}, \dots, x_1)$, the normalization condition is still satisfied.

4 Results and discussion

4.1 Hydrogen chains

We choose the 1D hydrogen chain as the first benchmark system to investigate the accuracy of the BDG-RNN and RBM-inspired correlator as well as the performance of the semistochastic algorithm for local energy. For this system, MPS offers a compact description of ground state entanglement,⁵⁴ and exact results are available⁵⁵ for comparison. All hydrogen atoms are equally spaced with a bond length of $R = 2.0a_0$. The STO-6G basis set and orthonormalized

atomic orbitals (OAOs) are used following the previous work.⁵⁵

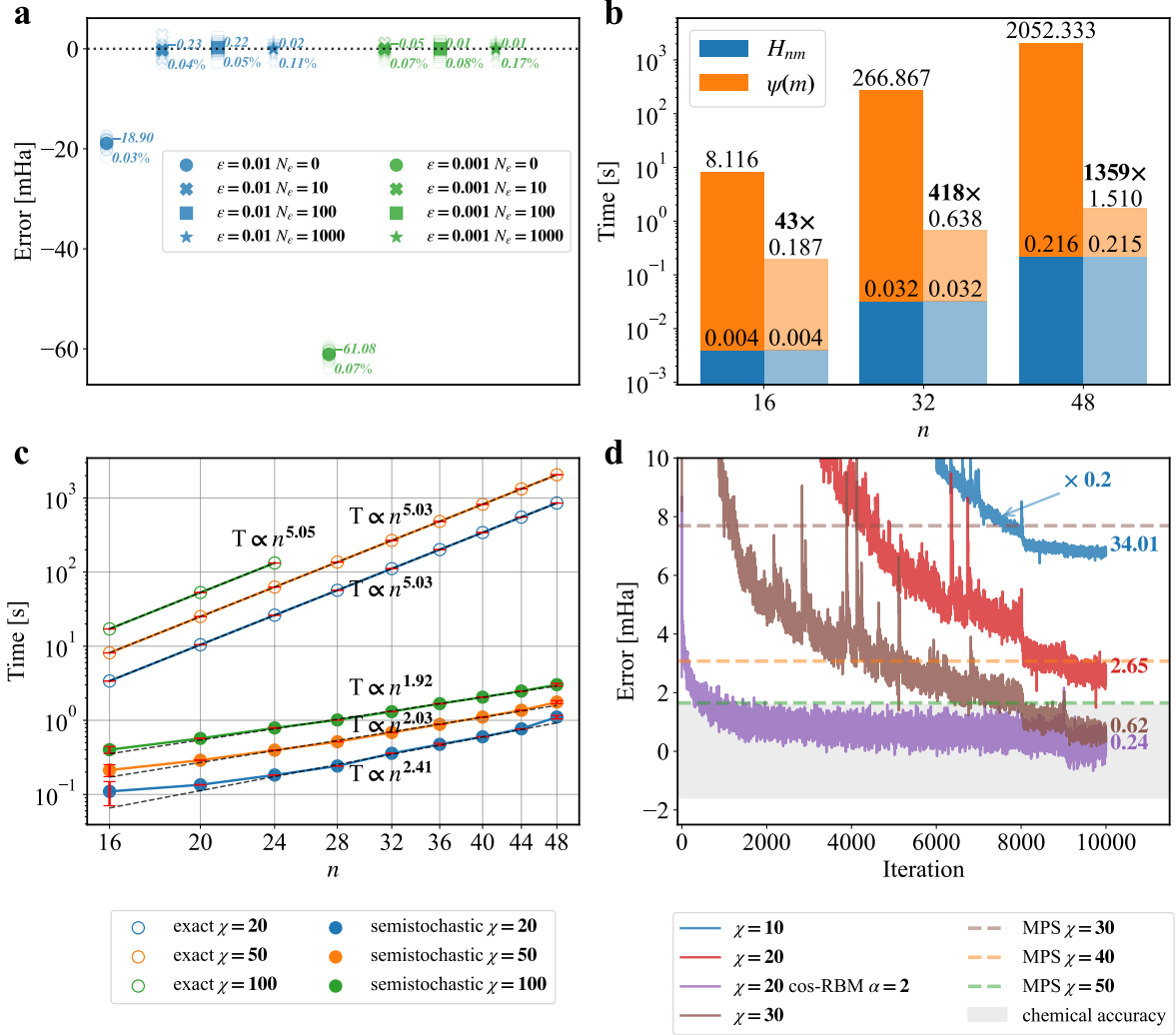


Figure 2: Results for the 1D hydrogen chains with a bond length of $2.00a_0$. **a**: Comparison of the performance of the semistochastic algorithm for local energy using different ϵ and N_ϵ for H_{50} using the BDG(1)-RNN ansatz with $\chi = 10$. The percentage of computational cost relative to the original algorithm is shown below each marker, and the error relative to the exact local energy is shown above the marker. Results are obtained using a fixed sample size of $N_s = 5 \times 10^4$. **b**: Detailed timing for local energy evaluations, including the evaluation of matrix elements H_{nm} and wavefunction $\psi(m)$ at $\chi = 50$. The number of sample N_s is fixed at 2048. The dark-colored and light-colored bars represent the original and the semistochastic algorithm with $\epsilon = 0.01$ and $N_\epsilon = 100$. The speed-up ratio for wavefunction computation is indicated above the light-colored bars. **c**: Timing for local energy evaluations as a function of the chain lengths (from H_{16} to H_{48}). The number of sample N_s is fixed at 2048, while the bond dimensions χ are set to 20, 50 and 100. **d**: Energy convergence for variational optimization with different χ and $N_s = 2 \times 10^5$. The shaded regions indicates the chemistry accuracy (1 kcal/mol).

Figure 2a illustrates the behaviour of the semistochastic algorithm for local energy with respect to the choices of ϵ and N_ϵ for H_{50} . We find that the mean energy converges systematically towards the exact value (black) with decreasing variance as N_ϵ increases. Note that the results obtained with $N_\epsilon = 0$ exhibit a large bias. To strike a balance between computational efficiency and accuracy, we will use $\epsilon = 0.01$ and $N_\epsilon = 100$ in optimization. With these settings, the computational cost is reduced to just 0.05% of the original, yielding an approximately 2000-fold speedup. Furthermore, to analyze the computational scaling for the evaluation of local energy, we investigate the 1D hydrogen chains with three different sizes (H_{16} , H_{32} , and H_{48}). Figure 2b presents the detailed breakdown for the computational time, including both the computation of Hamiltonian matrix elements and wavefunctions. Notably, the computation of matrix elements requires significantly less time than the wavefunction computation. Compared to the original scheme, the semistochastic algorithm achieves a speedup ratio of 43, 418, and 1359 for the wavefunction calculation. The result of the computational scaling is summarized in Fig. 2c for different chain lengths. The scaling of the exact local energy evaluation is $\mathcal{O}(K^5)$, as the evaluation of the BDG(1)-RNN ansatz scales as $\mathcal{O}(\chi^2 K)$ and the number of non-zero matrix elements is $\mathcal{O}(K^4)$. In contrast, the semistochastic evaluation achieves a significant reduction in scaling, which decreases from $\mathcal{O}(K^5)$ to approximately $\mathcal{O}(K^2)$. Note that the scaling continues to decrease as χ increases, which results from the fact that the proportion of wavefunction evaluation becomes more dominant with increasing χ .

We now investigate the optimization of the BDG(1)-RNN ansatz as a function of the bond dimension χ using the H_{50} chain. Figure 2d shows the energy convergence throughout the optimization iterations. The BDG(1)-RNN ansatz demonstrates better accuracy compared to MPS at the same χ . For example, BDG(1)-RNN at $\chi = 30$ yields an energy error 0.6 mHa, whereas MPS calculations require $\chi > 50$ to attain the same level of accuracy. This is likely due to the increased variational degree of freedoms in the ansatz. To further enhance the accuracy, we apply the correlation factor cos-RBM($\alpha = 2$) for $\chi = 20$, with its parameters

partially initialized from the result of the optimized BDG(1)–RNN. This approach further reduces the energy error to 0.2 mHa, whereas the energy error for BDG–RNN without the correlation factor is 2.6 mHa. Note that the parameters of BDG(1)–RNN are 46100 ($\chi = 10$), 172100 ($\chi = 20$), and 378100 ($\chi = 30$), while BDG(1)–RNN ($\chi = 20$) with cos-RBM($\alpha = 2$) contains 192300 parameters. Therefore, the improvement in accuracy is achieved with only 20200 additional parameters compared to the original BDG(1)–RNN ansatz.

4.2 Iron–sulfur cluster $[\text{Fe}_2\text{S}_2(\text{SCH}_3)_4]^{2-}$

Due to the large number of d -orbital electrons and different kinds of spin and charge fluctuations,^{56,57} iron-sulfur clusters are typical examples for strongly correlated systems. In this work, we selected the previously investigated $[\text{Fe}_2\text{S}_2(\text{SCH}_3)_4]^{2-}$ as the benchmark system with a CAS(30e, 20o) model, where the active space and integrals⁵⁷ were available online.⁵⁸ To reduce orbital entanglement, we use the entanglement-minimized orbitals (EMOs) obtained using spin-adapted MPS with $\chi = 100$.⁵⁹ Figure 3a illustrates the topological structures of the BDG(1)–RNN and BDG(2)–RNN architectures. In Fig. 3b, we compare the performance of the semistochastic algorithm for local energy using different ϵ and N_ϵ for the BDG(1)–RNN ansatz with $\chi = 50$. Based on these results, we selected $\epsilon = 0.01$ and $N_\epsilon = 1000$ by balancing computational accuracy, precision, and efficiency, which reduces the computational cost by roughly an order of magnitude compared to the original scheme.

We present the energy convergence as a function of the bond dimension χ and the number of variational parameters in Figs. 3c and 3d, respectively. Similarly to the hydrogen chain, BDG(1)–RNN shows a marked reduction in energy error compared to the standard MPS with identical bond dimensions χ . At $\chi = 200$, BDG(1)–RNN achieves chemical accuracy (1 kcal/mol), while standard MPS requires $\chi = 400$ to achieve a comparable accuracy. Compared to BDG(1)–RNN, BDG(2)–RNN demonstrates a slight improvement on the energy error at the same χ . A large improvement is achieved by incorporating the cos-RBM correlator with the parameters α set to 2. At $\chi = 100$, the cos-RBM achieves an error

of 1.7 mHa (approaching chemical accuracy), outperforming the BDG(1)–RNN result (3.0 mHa). Increasing the bond dimension to $\chi = 200$ further reduces the cos-RBM error to 1.1 mHa. Finally, the more sophisticated correlator Ising-RBM with the parameter $\alpha = 2$ yields additional gains in accuracy at the same χ and the number of parameters. In particular, it reaches the chemical accuracy when $\chi = 100$.

4.3 Three-dimensional $3 \times 3 \times 2$ hydrogen cluster H_{18}

To examine the potential of the BDG–RNN ansatz and RBM-inspired correlator, we select a more challenging 3D system — a $3 \times 3 \times 2$ hydrogen cluster H_{18} , where MPS require much larger bond dimensions (χ) to accurately capture the entanglement of the system. We set the interatomic distance to $4.0a_0$ between the nearest-neighbour hydrogen atoms. The OAOs obtained in the STO-3G basis are ordered with the Fiedler ordering^{43,44} for the calculations using MPS and BDG(k)–RNN ($k \leq 3$). The topologies of BDG–RNN are illustrated in Fig. 4a. For local energy evaluation, we systematically tested the hyperparameters ϵ and N_ϵ in Fig. 4b. The choice of $\epsilon = 0.01$ and $N_\epsilon = 100$ achieves approximately an 80-fold speedup compared to the original algorithm, while maintaining energy errors below 0.1 mHa, indicating a good trade-off between computational efficiency and accuracy.

In Fig. 4c, we evaluate the performance of correlators on top of BDG(3)–RNN with $\chi = 40$, including cos-RBM, Ising-RBM, Jastrow ($f_{\text{Jastrow}}(n) = e^{\sum_{ij}^{2K} W_{ij} n_i n_j}$ with $(W_{ij}) \in \mathbb{R}^{2K \times 2K}$), and a multilayer perceptron (MLP) defined by

$$f_{\text{mlplike}}(n) = \prod_{k=1}^{h_2} \cos \left(b_{1,k} + 2\pi \sum_{j=1}^{h_1} W_{1,jk} \cdot f_0(b_{0,j} + \sum_i^{2K} W_{0,ij} n_i) \right), \quad (25)$$

where $(W_{0,ij}) \in \mathbb{R}^{2K \times h_1}$ and $(W_{1,jk}) \in \mathbb{R}^{h_1 \times h_2}$ are real weights matrices ($h_1 = 4K$ and $h_2 = 4K$), while $(b_{0,j}) \in \mathbb{R}^{h_1}$ and $(b_{1,k}) \in \mathbb{R}^{h_2}$ are bias vectors, and the activation function is chosen as $f_0(z) = z^2 + z$. All these correlation factors significantly improve the accuracy, with the Ising-RBM demonstrating the best performance among them. In addition, we

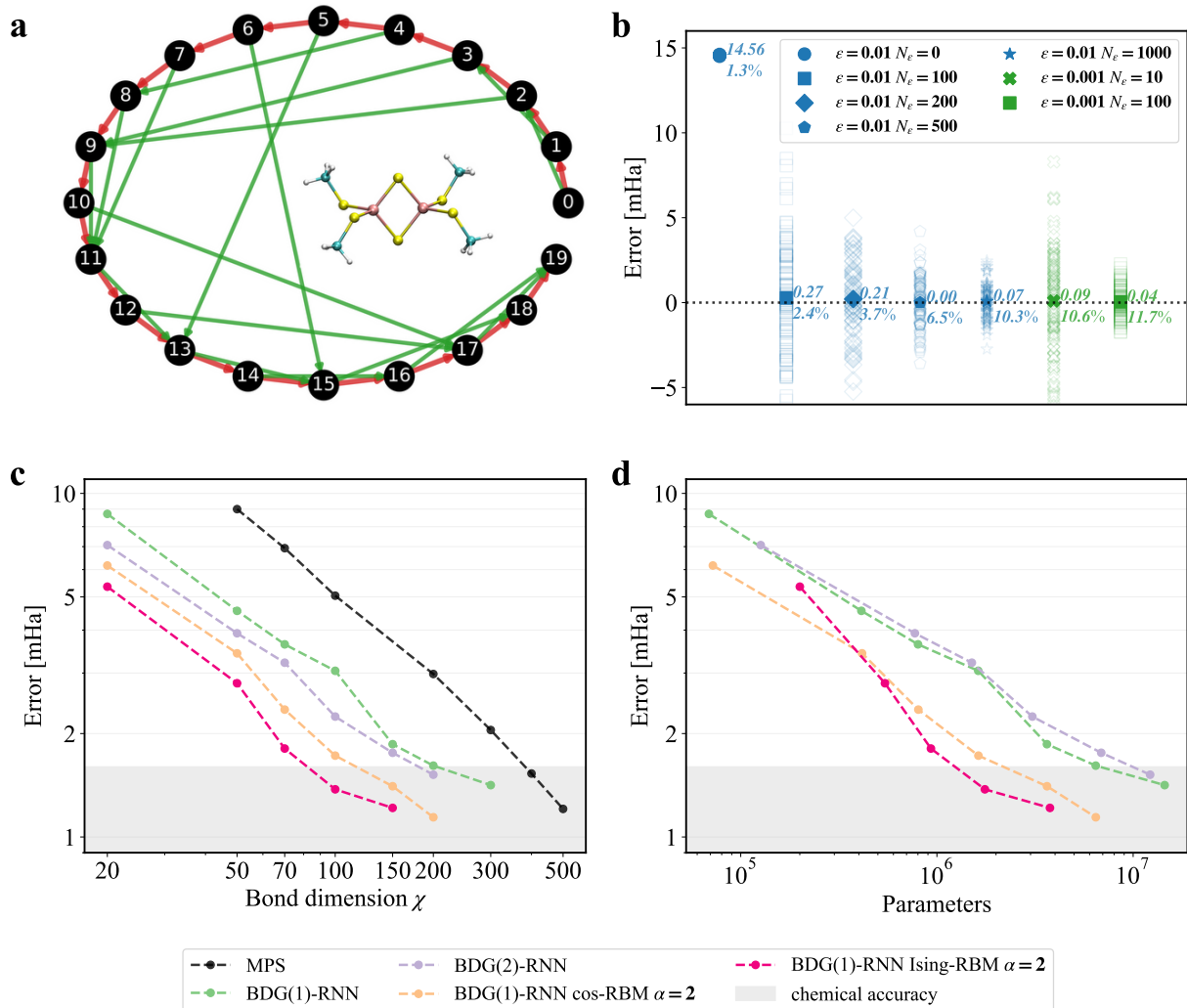


Figure 3: Results for the CAS(30e,20) model of the iron-sulfur cluster $[\text{Fe}_2\text{S}_2(\text{SCH}_3)_4]^{2-}$. **a**: Illustration of the topology of BDG(1)-RNN and BDG(2)-RNN. The red arrows represent BDG(1)-RNN (=MPS-RNN), while the green arrows represent the additional edges in BDG(2)-RNN. **b**: Assessment of the accuracy, precision, and efficient the semistochastic algorithm for local energy with different hyperparameters ϵ and N_ϵ using the BDG(1)-RNN ansatz with $\chi = 50$ and a sample size of $N_s = 10^7$. The error relative to the exact local energy is shown above each marker, and the percentage of computational cost relative to the original algorithm is shown below. **c,d**: Energy convergence with respect to the bond dimension χ and the number of variational parameters for BDG-RNN with and without the cos-RBM and Ising-RBM correlators obtained using $N_s = 10^7$. The exact energy is taken from Ref. ⁵⁷

investigated the effects of increasing α in cos-RBM and Ising-RBM in Fig. 4d. At $\alpha = 2$, the Ising-RBM parameters are derived from further optimization of the cos-RBM. For $\alpha > 2$, parameters were updated utilizing the optimized parameters from the preceding α as initial conditions. We observe that as α increases, the energy error further decreases slightly. Notably, when $\alpha = 16$, the energy errors of cos-RBM and Ising-RBM converge to nearly identical values.

We compare the convergence behaviors of MPS and BDG-RNN in Figs. 4e and 4f, respectively. MPS demonstrates slow convergence toward the ground state energy with increasing bond dimension, requiring $\chi > 500$ to achieve the chemical accuracy. The energy of BDG(1)-RNN also exhibits slow convergence, although its error is systematically smaller compared to that of the MPS. Compared with BDG(1)-RNN, both BDG(2)-RNN and BDG(3)-RNN show significantly faster convergence with the increasing bond dimension. For example, the energy error of BDG(3)-RNN approaches 1.1 mHa at $\chi = 250$, achieving the chemical accuracy. Compared with BDG(2)-RNN, BDG(3)-RNN does not exhibit significant improvement over BDG(2)-RNN, which is likely due to the quasi-3D structure of the molecule. We integrate the cos-RBM and Ising-RBM correlators with $\alpha = 2$ into the BDG(3)-RNN. With the correlation factors, the same accuracy as the previous BDG(3)-RNN at $\chi = 250$ can now be achieved at a reduced $\chi = 150$. We also examine the inclusion of the tensor terms into BDG(2)-RNN, denoted BDG(2)-TensorRNN. Notably, BDG(2)-TensorRNN achieves accuracy comparable to BDG(3)-RNN at $\chi = 250$ with a reduced bond dimension of $\chi = 100$, while the number of variational parameters for reaching the chemical accuracy is also significantly reduced.

5 Conclusion

In this work, we propose a bounded-degree graph RNN (BDG-RNN) ansätze, which can represent complex entanglement structures in molecular systems using the RNN framework.

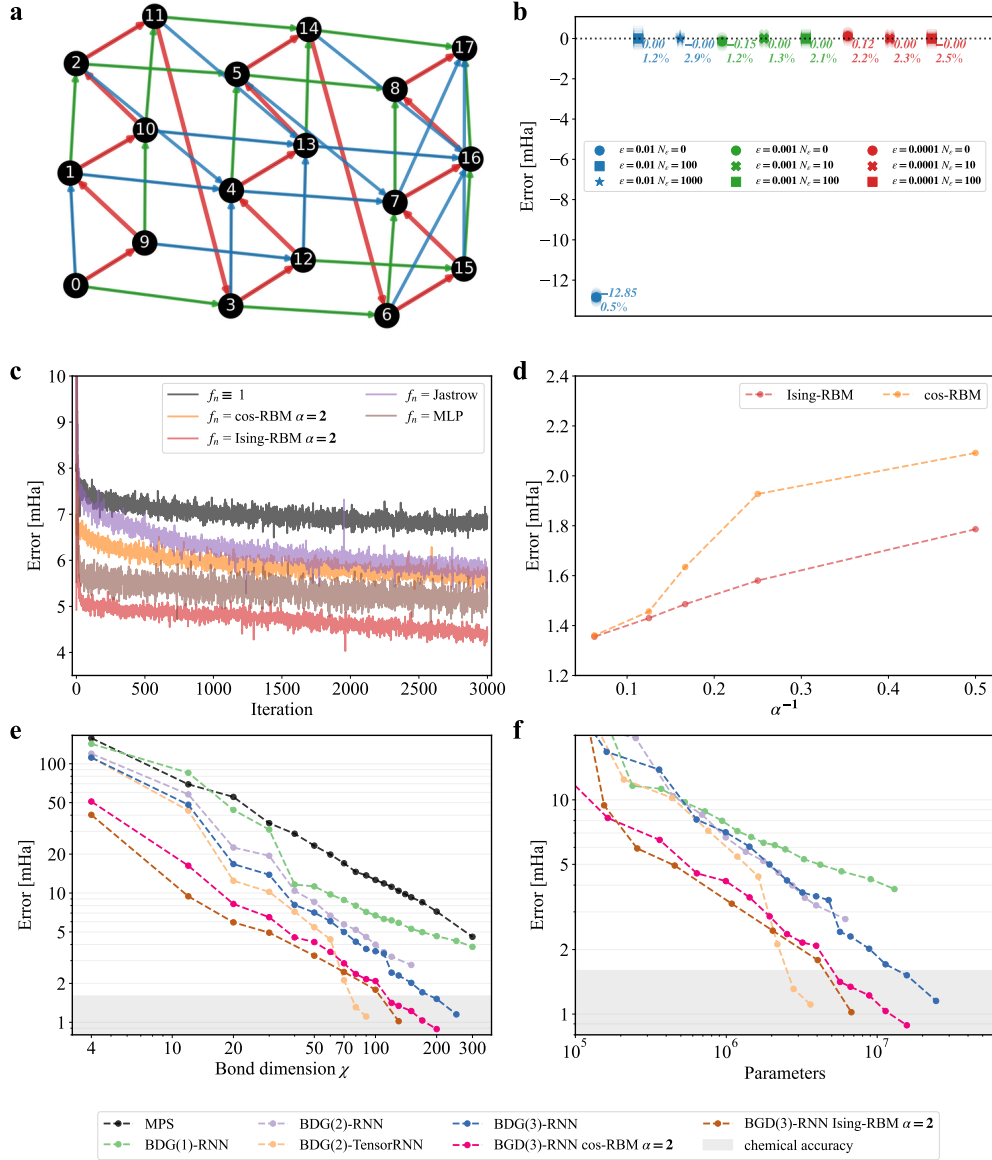


Figure 4: Results for the three-dimensional $3 \times 3 \times 2$ hydrogen clusters H_{18} . **a:** Illustration of the topologies of the BDG-RNN variants. Red edges denote the base BDG(1)-RNN structure, green edges represent the additional edges in BDG(2)-RNN, while blue edges indicate the additional edges in BDG(3)-RNN. **b:** Assessment of the accuracy, precision, and efficiency of the semistochastic algorithm for local energy with different hyperparameters ϵ and N_ϵ using the BDG(3)-RNN ansatz with $\chi = 100$ and a sample size of $N_s = 2 \times 10^5$. The error with respect to the exact local energy is shown above each marker. In later calculations, the values of ϵ and N_ϵ are set to 0.01 and 100, respectively. **c:** The optimization process for different correlators (cos-RBM, Ising-RBM, Jastrow and MLP) using BDG(3)-RNN with $\chi = 40$. The reference energy is taken from the MPS energy with $\chi = 2000$. **d:** Absolute error of energy (mHa) as a function of α^{-1} using cos-RBM and Ising-RBM correlators on top of BDG(3)-RNN with $\chi = 100$. **e, f:** Energy convergence with respect to the bond dimension χ and the number of variational parameters for BDG-RNN with and without the cos-RBM and Ising-RBM correlators obtained using $N_s = 10^6$.

BDG-RNN can be initialized using the MPS parameters, alleviating the optimization difficulties caused by random initialization parameters. To further improve the accuracy, we introduce RBM-inspired correlators (cos-RBM and Ising-RBM variants) that significantly enhance NQS expressivity, while remaining full compatibility with the autoregressive sampling via reweighting technique. Additionally, we introduce a semistochastic scheme for local energy evaluation that significantly reduces computational costs without significantly affecting accuracy. These ansätze and techniques are implemented in the open-source PYNQS⁴⁹ package, which facilitates the exploration of NQS methodologies. We validated our methodology on several prototypical systems, including the 1D hydrogen chain H_{50} , the iron-sulfur cluster $[Fe_2S_2(SCH_3)_4]^{2-}$ with the CAS(30e, 20o) active space, and the more challenging 3D $3 \times 3 \times 2$ hydrogen cluster H_{18} , where the chemical accuracy is achieved across all systems using BDG-RNN. In particular, a large systematic enhancement in accuracy is observed using RBM-inspired correlators.

While BDG-RNN demonstrates superior accuracy over MPS at the same bond dimensions, further developments are necessary in order to apply it to large-scale strongly correlated systems. These include incorporating established techniques for using symmetry and mixed precision schemes, which would substantially reduce both memory requirements and computational costs. In addition, future work will also apply advanced optimization techniques such as minimum-step stochastic reconfiguration,^{21,60} which could significantly accelerate the VMC optimization. We hope that the algorithms and software presented in this work will stimulate future developments in state-of-the-art NQS methods for quantum chemistry.

Acknowledgement

This work was supported by the Innovation Program for Quantum Science and Technology (Grant No. 2023ZD0300200) and the Fundamental Research Funds for the Central Universities.

Supporting Information Available

Detailed algorithms, derivation of the energy gradient in the presence of correlators, values of $B = \langle |f_n|^2 \rangle$ for different molecules.

References

- (1) Grimme, S. Improved second-order Møller–Plesset perturbation theory by separate scaling of parallel- and antiparallel-spin pair correlation energies. J. Chem. Phys. **2003**, 118, 9095–9102.
- (2) Werner, H.-J.; Knowles, P. J. An efficient internally contracted multiconfiguration–reference configuration interaction method. J. Chem. Phys. **1988**, 89, 5803–5814.
- (3) Bartlett, R. J.; Musiał, M. Coupled-cluster theory in quantum chemistry. Rev. Mod. Phys. **2007**, 79, 291–352.
- (4) Kohn, W.; Becke, A. D.; Parr, R. G. Density functional theory of electronic structure. J. Chem. Phys. **1996**, 100, 12974–12980.
- (5) Ceperley, D.; Chester, G. V.; Kalos, M. H. Monte Carlo simulation of a many-fermion study. Phys. Rev. B **1977**, 16, 3081.
- (6) Toulouse, J.; Assaraf, R.; Umrigar, C. J. Adv. Quantum Chem.; Elsevier, 2016; Vol. 73; pp 285–314.
- (7) Austin, B. M.; Zubarev, D. Y.; Lester Jr, W. A. Quantum Monte Carlo and related approaches. Chem. Rev. **2012**, 112, 263–288.
- (8) Kalos, M. H. Monte Carlo calculations of the ground state of three- and four-body nuclei. Phys. Rev. **1962**, 128, 1791.

- (9) Sorella, S. Green function Monte Carlo with stochastic reconfiguration. Phys. Rev. Lett. **1998**, 80, 4558.
- (10) Motta, M.; Zhang, S. Ab initio computations of molecular systems by the auxiliary-field quantum Monte Carlo method. WIREs Comput. Mol. Sci. **2018**, 8, e1364.
- (11) Lee, J.; Pham, H. Q.; Reichman, D. R. Twenty years of auxiliary-field quantum Monte Carlo in quantum chemistry: An overview and assessment on main group chemistry and bond-breaking. J. Chem. Theory Comput. **2022**, 18, 7024–7042.
- (12) Carleo, G.; Troyer, M. Solving the quantum many-body problem with artificial neural networks. Science **2017**, 355, 602–606.
- (13) Hermann, J.; Spencer, J.; Choo, K.; Mezzacapo, A.; Foulkes, W. M. C.; Pfau, D.; Carleo, G.; Noé, F. Ab initio quantum chemistry with neural-network wavefunctions. Nat. Rev. Chem. **2023**, 7, 692–709.
- (14) Hibat-Allah, M.; Ganahl, M.; Hayward, L. E.; Melko, R. G.; Carrasquilla, J. Recurrent neural network wave functions. Phys. Rev. Res. **2020**, 2, 023358.
- (15) Wu, D.; Rossi, R.; Vicentini, F.; Carleo, G. From tensor-network quantum states to tensorial recurrent neural networks. Phys. Rev. Res. **2023**, 5, L032001.
- (16) Choo, K.; Neupert, T.; Carleo, G. Two-dimensional frustrated J1-J2 model studied with neural network quantum states. Phys. Rev. B **2019**, 100, 125124.
- (17) Barrett, T. D.; Malyshev, A.; Lvovsky, A. Autoregressive neural-network wavefunctions for ab initio quantum chemistry. Nat. Mac. Intell. **2022**, 4, 351–358.
- (18) Chen, Z.; Newhouse, L.; Chen, E.; Luo, D.; Soljagic, M. Antn: Bridging autoregressive neural networks and tensor networks for quantum many-body simulation. Adv. Neural Inf. Process. Syst. **2023**, 36, 450–476.

- (19) Zhang, Y.-H.; Di Ventra, M. Transformer quantum state: A multipurpose model for quantum many-body problems. Phys. Rev. B **2023**, 107, 075147.
- (20) Wu, Y.; Guo, C.; Fan, Y.; Zhou, P.; Shang, H. NNQS-transformer: an efficient and scalable neural network quantum states approach for ab initio quantum chemistry. Proceedings of the International Conference for High Performance Computing, Networking, Storage and Analysis. 2023; pp 1–13.
- (21) Rende, R.; Viteritti, L. L.; Bardone, L.; Becca, F.; Goldt, S. A simple linear algebra identity to optimize Large-Scale Neural Network Quantum States. Commun. Phys. **2024**, 7.
- (22) Knitter, O.; Zhao, D.; Stokes, J.; Ganahl, M.; Leichenauer, S.; Veerapaneni, S. Retentive neural quantum states: efficient ansätze for ab initio quantum chemistry. Mach. Learn.: Sci. Technol. **2025**, 6, 025022.
- (23) Liu, A.-J.; Clark, B. K. Neural network backflow for ab-initio quantum chemistry. Phys. Rev. B **2024**, 110, 115137.
- (24) Kan, B.; Tian, Y.; Wu, Y.; Zhang, Y.; Shang, H. Bridging the Gap between Transformer-Based Neural Networks and Tensor Networks for Quantum Chemistry. J. Chem. Theory Comput. **2025**, 21, 3426–3439.
- (25) Du, S.-J.; Chan, G. K. Neuralized Fermionic Tensor Networks for Quantum Many-Body Systems. arXiv preprint arXiv:2506.08329 **2025**,
- (26) Li, X.; Huang, J.-C.; Zhang, G.-Z.; Li, H.-E.; Cao, C.-S.; Lv, D.; Hu, H.-S. Non-stochastic Optimization Algorithm for Neural-network Quantum States. J. Chem. Theory Comput. **2023**, 19, 8156–8165.
- (27) Li, X.; Huang, J.-C.; Zhang, G.-Z.; Li, H.-E.; Shen, Z.-P.; Zhao, C.; Hu, H.-S. Improved

- Optimization for the Neural-network Quantum States and Tests on the Chromium Dimer. J. Chem. Phys. **2024**, 160.
- (28) Liu, A.-J.; Clark, B. K. Efficient optimization of neural network backflow for ab-initio quantum chemistry. arXiv preprint arXiv:2502.18843 **2025**,
- (29) Zhao, T.; Stokes, J.; Veerapaneni, S. Scalable neural quantum states architecture for quantum chemistry. Mach. Learn.: Sci. Technol. **2023**, 4, 025034.
- (30) Schwarz, L. R.; Alavi, A.; Booth, G. H. Projector Quantum Monte Carlo Method for Nonlinear Wave Functions. Phys. Rev. Lett. **2017**, 118, 176403.
- (31) Wei, H.; Neuscamman, E. Reduced scaling Hilbert space variational Monte Carlo. J. Chem. Phys. **2018**, 149.
- (32) Sabzevari, I.; Sharma, S. Improved speed and scaling in orbital space variational Monte Carlo. J. Chem. Theory Comput. **2018**, 14, 6276–6286.
- (33) Levin, D. A.; Peres, Y. Markov chains and mixing times; American Mathematical Soc., 2017; Vol. 107.
- (34) Griewank, A.; Walther, A. Evaluating derivatives: principles and techniques of algorithmic differentiation; SIAM, 2008.
- (35) Robbins, H.; Monro, S. A stochastic approximation method. Ann. Math. Statist. **1951**, 400–407.
- (36) Kingma, D. P.; Ba, J. Adam: A method for stochastic optimization. International Conference on Learning Representations. 2015.
- (37) Loshchilov, I.; Hutter, F. Fixing Weight Decay Regularization in Adam. International Conference on Learning Representations. 2019.

- (38) Nomura, Y.; Darmawan, A. S.; Yamaji, Y.; Imada, M. Restricted Boltzmann machine learning for solving strongly correlated quantum systems. Phys. Rev. B **2017**, 96, 205152.
- (39) Choo, K.; Mezzacapo, A.; Carleo, G. Fermionic neural-network states for ab-initio electronic structure. Nat. Commun. **2020**, 11, 1–7.
- (40) Hibat-Allah, M.; Ganahl, M.; Hayward, L. E.; Melko, R. G.; Carrasquilla, J. Recurrent neural network wave functions. Phys. Rev. Res. **2020**, 2, 023358.
- (41) Chung, J.; Gulcehre, C.; Cho, K.; Bengio, Y. Empirical evaluation of gated recurrent neural networks on sequence modeling. arXiv preprint arXiv:1412.3555 **2014**,
- (42) Hochreiter, S.; Schmidhuber, J. Long short-term memory. Neural Comput. **1997**, 9, 1735–1780.
- (43) Barcza, G.; Legeza, Ö.; Marti, K. H.; Reiher, M. Quantum-information analysis of electronic states of different molecular structures. Phys. Rev. A **2011**, 83, 012508.
- (44) Olivares-Amaya, R.; Hu, W.; Nakatani, N.; Sharma, S.; Yang, J.; Chan, G. K. The ab-initio density matrix renormalization group in practice. J. Chem. Phys. **2015**, 142.
- (45) Tucker, L. R. Some mathematical notes on three-mode factor analysis. Psychometrika **1966**, 31, 279–311.
- (46) Deng, D.-L.; Li, X.; Das Sarma, S. Quantum entanglement in neural network states. Phys. Rev. X **2017**, 7, 021021.
- (47) Yang, P.-J.; Sugiyama, M.; Tsuda, K.; Yanai, T. Artificial Neural Networks Applied as Molecular Wave Function Solvers. J. Chem. Theory Comput. **2020**, 16, 3513–3529.
- (48) Becca, F.; Sorella, S. Quantum Monte Carlo approaches for correlated systems; Cambridge University Press, 2017.

- (49) <https://github.com/Quantum-Chemistry-Group-BNU/PyNQS>.
- (50) Paszke, A.; Gross, S.; Massa, F.; Lerer, A.; Bradbury, J.; Chanan, G.; Killeen, T.; Lin, Z.; Gimelshein, N.; Antiga, L., et al. Pytorch: An imperative style, high-performance deep learning library. Adv. Neural Inf. Process. Syst. **2019**, 32.
- (51) Li, Z. Expressibility of comb tensor network states (CTNS) for the P-cluster and the FeMo-cofactor of nitrogenase. Electron. Struct. **2021**, 3, 014001.
- (52) Xiang, C.; Jia, W.; Fang, W.-H.; Li, Z. Distributed Multi-GPU Ab Initio Density Matrix Renormalization Group Algorithm with Applications to the P-Cluster of Nitrogenase. J. Chem. Theory Comput. **2024**, 20, 775–786.
- (53) Sun, Q.; Zhang, X.; Banerjee, S.; Bao, P.; Barbry, M.; Blunt, N. S.; Bogdanov, N. A.; Booth, G. H.; Chen, J.; Cui, Z.-H., et al. Recent developments in the PySCF program package. J. Chem. Phys. **2020**, 153.
- (54) Schollwöck, U. The density-matrix renormalization group in the age of matrix product states. Ann. Phys. **2011**, 326, 96–192.
- (55) Hachmann, J.; Cardoen, W.; Chan, G. K. Multireference correlation in long molecules with the quadratic scaling density matrix renormalization group. J. Chem. Phys. **2006**, 125.
- (56) Sharma, S.; Chan, G. K. Communication: A flexible multi-reference perturbation theory by minimizing the Hylleraas functional with matrix product states. J. Chem. Phys. **2014**, 141.
- (57) Li, Z.; Chan, G. K.-L. Spin-projected matrix product states: Versatile tool for strongly correlated systems. J. Chem. Theory Comput. **2017**, 13, 2681–2695.
- (58) <http://github.com/zhendongli2008/Active-space-model-for-Iron-Sulfur-Clusters>, 2017.

- (59) Li, Z. Entanglement-minimized orbitals enable faster quantum simulation of molecules. arXiv preprint arXiv:2506.13386 **2025**,
- (60) Chen, A.; Heyl, M. Efficient optimization of deep neural quantum states toward machine precision. Nat. Phys. **2024**, 20, 1381–1382.

TOC Graphic

